



# The mechanical response of commercially pure copper under multiaxial loading at low and high strain rates

Junyi Zhou<sup>a</sup>, Yuan Xu<sup>a,\*</sup>, Maureen Aceves Lopez<sup>a</sup>, Lukasz Farbaniec<sup>a</sup>, Sophoclis Patsias<sup>b</sup>, Duncan Macdougall<sup>b</sup>, Julian Reed<sup>a</sup>, Nik Petrinic<sup>a</sup>, Daniel Eakins<sup>a</sup>, Clive Siviour<sup>a</sup>, Antonio Pellegrino<sup>a,\*</sup>

<sup>a</sup> Department of Engineering Science, University of Oxford, Oxford OX1 3PJ, United Kingdom

<sup>b</sup> Rolls-Royce PLC, PO Box 31, Derby, DE24 8BJ, UK

## ARTICLE INFO

### Keywords:

Split Hopkinson tension-torsion bar

Multiaxial failure

Failure stress envelope

Rate dependence

Commercially pure copper

## ABSTRACT

In this paper, we present the dynamic response of commercially pure copper subjected to combined tension-torsion loads representative of real case impact scenarios. Experiments were conducted both quasi statically, at a strain rate equal to  $10^{-3} \text{ s}^{-1}$ , and dynamically at strain rates in the region between  $500 \text{ s}^{-1}$  and  $1000 \text{ s}^{-1}$ . All high rate experiments were conducted using a novel Split Hopkinson Tension-Torsion Bar instrumented with high-speed photographic equipment. The dynamic combined loading experiments demonstrate the capability of the apparatus to generate longitudinal and torsional stress waves which are synchronised upon loading of the specimen. The presented data show that dynamic equilibrium conditions and nearly steady strain rates were achieved during the experiments. Additionally, the analyses of the loading paths show that nearly proportional strain loading was attained during testing.

The measured experimental results illustrate, for the first time, the failure stress locus of the material over a wide range of stress states including pure torsion, shear-dominated combined tension-shear, tension-dominated combined tension-shear and plain tension. The quasi-static and dynamic failure envelopes are herein presented in the normal stress vs shear stress space to motivate the development of accurate and effective constitutive models. To conclude, the Drucker-Prager criterion was employed to approximate the failure loci and to assess the rate sensitivity of the material. A moderate asymmetry of the uniaxial ultimate stresses in tension and compression is predicted both at quasi-static and dynamic strain rates.

## 1. Introduction

Copper (Cu) has been widely used in engineering due to its outstanding electrical/thermal conductivity, corrosion resistance, strength, and fatigue resistance. The literature includes extensive studies focusing on processing techniques enhancing strength and ductility of the material [1–6].

The quasi-static mechanical behaviour of Cu has been widely studied [6]. Sanders et al. [7] studied the effect of grain size on the quasi-static elastic tensile behaviour of nanocrystalline copper; Wang and Ma [8] tested pure Cu specimen in tension at various quasi-static strain rates (between  $10^{-6}$  and  $10^{-1} \text{ s}^{-1}$ ) and two temperature levels (77 K and 298 K) and they concluded that the yield strength is strain rate and temperature sensitive. Furthermore, Zhao et al. [9] performed quasi-static

simultaneous tension-torsion tests on pure Cu; however, they focused on the effect of stress-triaxiality on its microstructure and microhardness rather than on the mechanical response and on the failure stress and strain. For what concerns high strain rates experimentation, Lindholm et al. [10] developed a high-speed torsion testing machine to twist pure Cu specimen at strain rates up to  $330 \text{ s}^{-1}$ . Their experimental data showed a positive relationship between strain rates and flow stress. Tong et al. [11] conducted an experimental investigation on the high shear rate behaviour of Cu at rates of strain up to  $10^6 \text{ s}^{-1}$  under both constant strain rate and changing strain rate conditions. The flow stress was found to increase noticeably at strain rates of  $10^5 \text{ s}^{-1}$  or higher, whilst it decreases gradually following a sharp decrease in strain rate during variable strain rate experiments. Similarly, Gray III et al. [12] studied the influence of strain rate (between  $10^{-3}$  and  $4500 \text{ s}^{-1}$ ) and

\* Corresponding author.

E-mail addresses: [yuan.xu@eng.ox.ac.uk](mailto:yuan.xu@eng.ox.ac.uk) (Y. Xu), [antonio.pellegrino@eng.ox.ac.uk](mailto:antonio.pellegrino@eng.ox.ac.uk) (A. Pellegrino).

<https://doi.org/10.1016/j.ijmecsci.2022.107340>

Received 14 January 2022; Received in revised form 12 April 2022; Accepted 5 May 2022

Available online 10 May 2022

0020-7403/© 2022 The Author(s). Published by Elsevier Ltd. This is an open access article under the CC BY-NC-ND license (<http://creativecommons.org/licenses/by-nc-nd/4.0/>).

temperature (between 77 K and 298 K) on the compressive response of pure Cu. It was summarised that the flow stress and ultimate strength increases with increasing strain rate and decreasing temperature. Mishra et al. [13] measured the high-rate compressive response of ultrafine-grained Cu and reported a significant increment of the ultimate strength when the strain rate increased from the quasi static to the dynamic regime. Armstrong et al. [14] investigated the relationship between flow stress and strain rate of Cu over a wide range of strain rates ( $10^{-3}$  -  $10^7$  s $^{-1}$ ) under impact-induced shock tests and shockless tests and concluded that the plastic deformation rate dependence under these two kinds of loading can be attributed to the different type of dislocation movement induced. Nemat-Nasser and Li [15], and Tanner et al. [16] conducted compressive tests and numerical modelling on Oxygen Free High Conductivity (OFHC) Cu at various strain rates and temperatures and observed that the strain hardening of the material is strongly dependant on rate of deformation and temperature. More recently Dragnevski et al. [4] investigated the effect of undercooling rate and strain rate on the compressive yield stress of pure copper.

It is evident that the previous literature has investigated extensively the effects of microstructure, grain size, chemical composition, and temperature on the rate dependence of copper. However previous research on the dynamic behaviour of copper was conducted subjecting the material to a single loading mode, namely compression or shear, with the majority of the previous investigations focusing on the high rate compressive behaviour.

Per contra real impact loading case scenarios are rarely uniaxial and the mechanical response of engineering materials is generally dependant on the imposed stress state. For that reason, a thorough understanding of the dynamic behaviour of copper calls for the determination of the rate dependence, dynamic flow stress and failure envelope of the material undergoing various combined stress states.

The split Hopkinson pressure bar (SHPB) is the most popular technique to carry out high strain rates experiment due to its direct application of the unidirectional stress wave propagation theory for the evaluation of stress and strain in the specimen. It was first developed by Bertram Hopkinson in [17] and it has been extensively developed to explore the dynamic response of engineering materials [18–22]. Several authors measured the dynamic compressive properties of a wide range of materials such as ceramics, metals, woods, rocks, and polymers [23–29] using the SHPB. This technique can also be modified to conduct dynamic tension experiments [30]. The different split Hopkinson tension bar (SHTB) architectures can be categorised on the basis of the methodology employed to generate the tensile loading pulse. The most popular technique involves the direct impact of a tubular striker on the flanged end of the incident bar to generate the tensile wave [31–32]. This approach offers the advantage of controlling the rise time of the applied stress waves by means of pulse shaping techniques [33]. An alternative method to generate the tensile pulse relies on the rapid release of the tensile elastic energy stored in a section of the incident bar [34]. This methodology favours an easy alteration between tensile and compressive loading, and the possibility of combining tensile/compressive loading with shear loading. More recently a bespoke modified SHPB apparatus was used to measure the dynamic tensile response of composites, high performance fibres and brittle materials [35].

Torsional Hopkinson bar (SHToB) apparatuses were developed by [36–40] amongst the others. Most SHToB apparatuses adopt the pre-stored energy loading mechanism in which the desired torsional elastic energy is stored in the portion of the incident bar comprised between a rotary actuator and a clamp. The shear stress pulse is then generated by the rapid release of the clamp.

In the present work, we present, for the first time, the rate dependant response of commercially pure copper under concurrent tension-torsion loading. Experiments were carried out both quasi statically, at a strain rate equal to  $10^{-3}$  s $^{-1}$ , and dynamically at strain rates in the region between 500 s $^{-1}$  and 1000 s $^{-1}$ . Dynamic experiments were conducted using a purposely developed Split Hopkinson Tension-Torsion Bar

instrumented with high-speed imaging equipment. The apparatus generates simultaneous tensile and torsional stress waves in a single experiment, by employing both longitudinal and torsional actuators at the far-end of the incident bar and releasing the stored elastic energy by the rapid disengagement of a clamp. The measured experimental results delineate a locus identifying the failure of the material under different combinations of axial and shear stress. The quasi-static and dynamic failure loci are displayed in the direct-shear stress space to motivate the assessment of existing theoretical models and inspire the development of new constitutive laws. The Drucker-Prager criterion is employed to approximate the failure envelopes and to assess the rate sensitivity of the material. A moderate asymmetry of the uniaxial ultimate stresses in tension and compression is predicted both at quasi-static and dynamic strain rates. The failure surface of samples tested in different loading conditions is examined and analysed.

## 2. Material and specimen

The material investigated in this study is commercially pure Cu (99.9% purity). Details of the specimen geometry are illustrated in Fig. 1a. The specimen was machined from a bar to a thin-walled tube of total length equal to 40 mm. The gauge section of the specimen is characterised by a length equal to 2 mm, a wall thickness of 0.25 mm and external diameter equal to 15 mm.

All samples were manufactured using water-based semisynthetic coolants to prevent excessive heat generation and tooling wear during machining. Similar specimen geometries were successfully adopted in [41] on 0.33 mm thick aluminium samples, in [42] on 0.3 mm thick Ti6Al4V high rate torsion specimens, and in [43] where repeatable shear stress-strain characteristics were measured on Ti3Al2.5V using a wall thickness of 0.3 mm and the evaluated results compared to those obtained using shear compression specimens.

The ends of the samples were machined to octagonal shape to mate the interfaces with the incident and transmitted bars (Fig. 1b) and enable the transmission of torque; specimens and bar ends were also threaded externally to engage with suitable collars and allow the transmission of tensile loading (Fig. 1b).

## 3. Experimental setup, test procedure and data analysis

### 3.1. Experimental setup and test procedure

Tensile, torsional, and combined tension-torsion tests at quasi static ( $10^{-3}$  s $^{-1}$ ) and dynamic strain rates (up to  $\approx 1400$  s $^{-1}$ ) were conducted. Quasi-static (QS) tests were carried out using a Zwick/Roell Z250 material testing machine. The deformation history of the samples loaded quasi statically was recorded using four iDs (Image Development System) UEye USB 3.0 cameras. These were located around the axis of the specimen, equally spaced at an angle of 90° to each other in the horizontal plane. Tensile and shear strains were evaluated using the Digital Image Correlation (DIC) technique. Strains were processed by means of the commercial software DaVis produced by LaVision<sup>1</sup>.

A schematic drawing of the Tension-Torsion Hopkinson pressure bar (TTHB) utilised during the high strain rate (HR) experiments, and the associated C-clamp, are shown in Fig. 2. The TTHB consists of a hydraulic linear actuator located on the far end of the incident bar to apply tensile loading, an electrical harmonic drive to apply torsional loading, and a rapid release clamp positioned close to the interface between the incident bar and the specimen. Since the tensile and torsional waves propagate at different velocities, it is crucial to position the clamp in close proximity to the specimen to minimize the delay between the tensile and the shear loading waves.

During dynamic experiments, the axis of the sample is positioned

<sup>1</sup> LaVisionUK Ltd, 2 Minton Place, Victoria Road, Bicester, UK.

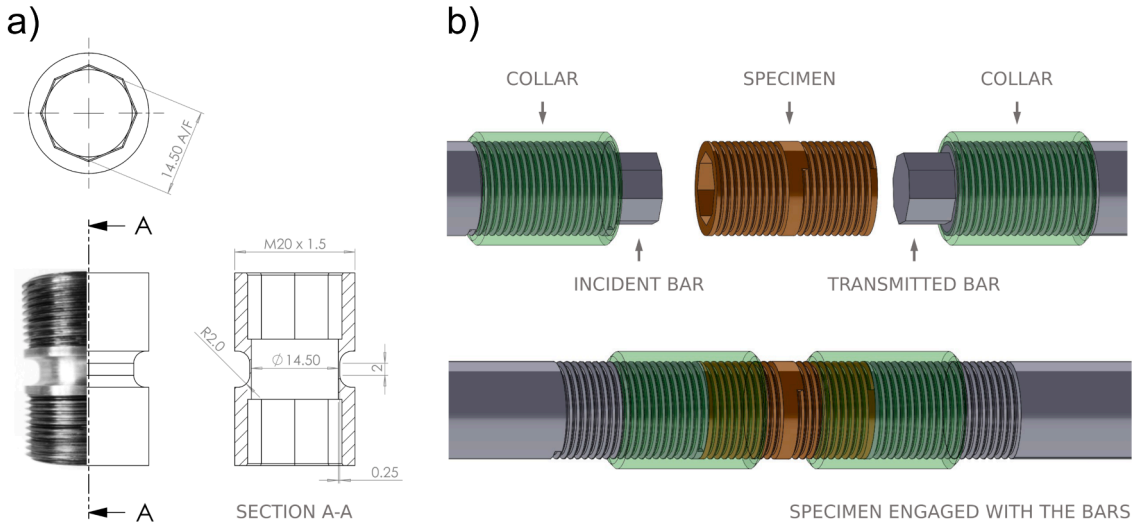


Fig. 1. (a) Pure Cu specimen with geometry details (all dimensions in mm); (b), schematic of the connection between specimen and bars.

horizontally, sandwiched between the incident and transmitted bars. These were made of aluminium alloy 7075-T6 and had diameter equal to 20 mm and length equal to 2500 mm. The tensile and torsional loading histories on the specimen were determined from the stress waves recorded by strain gauges mounted on the incident and transmitted bars. Two elements strain gauge rosettes (Tokyo Sokki Kenkyujo FCA-1-23) were used for the measurement of torsional loads and angular particle velocities. General use axial strain gauges (Tokyo Sokki Kenkyujo FLA-1-23) were used for the measurements of axial loads and longitudinal particle velocities. The tensile and shear strain gauges on the incident bar were positioned at a distance of 180 mm and 1063 mm from the interface with the specimen respectively. The distances between the specimen and the tensile and shear strain gauges on the transmitted bar were 345 mm and 575 mm, correspondingly. The C-shaped clamp was located in immediate proximity to the sample, 40 mm away from the interface between the specimen and the incident bar. A Photron SA5 high-speed camera and LaVision DaVis software were adopted to record high-speed footage and to conduct DIC analysis respectively. The camera was positioned perpendicularly to the axis of the sample.

C-clamp frame is in contact with the Hopkinson Bar base by means of a set of ball bearings. Thus, the frame can adjust its position ensuring that the load exerted by the jaws is symmetrical. The jaws are bolted together by a notched pin and are connected to the base by dowels that can slide along radial slots. To store tensile and torsional energies in the incident bar, the jaws are firstly pushed towards each other, clamping the bar, by a hydraulic ram; tension and torsion are then applied in sequence by the loading units. In this phase the clamping force generated by the ram is just below the value which fractures the pin. Subsequently the contact force is gradually increased by the hydraulic ram until the notched pin fractures; As a result, the jaws move away from each other releasing the clamp, thus generating tensile and torsional stress pulses. These propagate towards the specimen, deforming it. Because of the impedance mismatch between the incident bar and the specimen the two incident stress waves are partially reflected back to the incident bar and partially transmitted to the transmitted bar.

The testing procedure can be therefore summarised as follows: firstly, the cylindrical specimen is sandwiched between incident and transmitted bars. The clamp is then tightened to constrain the incident bar, after which tension and torsion are applied in sequence by the loading units. By fracturing the pin holding the clamp, the tensile and torsional waves are released rapidly, and propagate through the specimen. The strain gauge signals are recorded by a set of high-bandwidth amplifiers (Fylde H379TA transducer amplifiers) and digital oscilloscopes (Tektronix DPO 3034 digital phosphor oscilloscopes); high speed

cameras are triggered simultaneously and the recorded images synchronized with the strain gauges signals. More details on the working principle and the mechanical design can be found in [44].

### 3.2. Data analysis

*Evaluation of the tensile response.* Assuming 1-D wave propagation in slender rods, at the interface between incident bar and specimen, part of the incident wave  $\epsilon_I(t)$  is reflected ( $\epsilon_R(t)$ ) and part is transmitted to the transmitted bar as  $\epsilon_T(t)$ . The axial tensile loading on the incident and transmitted sides of the specimen is therefore:

$$F_1(t) = (EA)_I [\epsilon_I(t) + \epsilon_R(t)] \quad (1)$$

$$F_2(t) = (EA)_O \epsilon_T(t) \quad (2)$$

where the subscripts *I* and *O* denote the incident and transmitted bars respectively, *E* is the elastic modulus of the bars and *A* their cross section.

In conditions of dynamic equilibrium  $F_1 = F_2 = F$ , and the nominal tensile stress in the specimen is:

$$\sigma(t) = \frac{F(t)}{A_S} \quad (3)$$

where  $A_S$  is the cross-section of the thin-walled cylindrical specimen.

*Evaluation of the torsional response.* Similarly, the torque *T* on the two sides of the specimen can be evaluated as:

$$T_1(t) = \left( \frac{GJ}{r} \right)_I [\gamma_I(t) + \gamma_R(t)] \quad (4)$$

$$T_2(t) = \left( \frac{GJ}{r} \right)_O \gamma_T(t) \quad (5)$$

where  $\gamma_I(t)$ ,  $\gamma_R(t)$  and  $\gamma_T(t)$  are the incident, reflected and transmitted shear waves, *r* and *J* the radius and the polar moment of inertia of the bars, and *G* is their shear modulus. Again, in conditions of dynamic equilibrium  $T_1 = T_2 = T$ . The shear stress in the thin-walled specimen having a gauge section of mean radius  $r_s$  and polar moment of inertia  $J_S$  is therefore

$$\tau(t) = \frac{T(t)r_s}{J_S} \quad (6)$$

*Evaluation of dynamic equilibrium.* Longitudinal and torsional dynamic equilibrium conditions were achieved during the experiments.

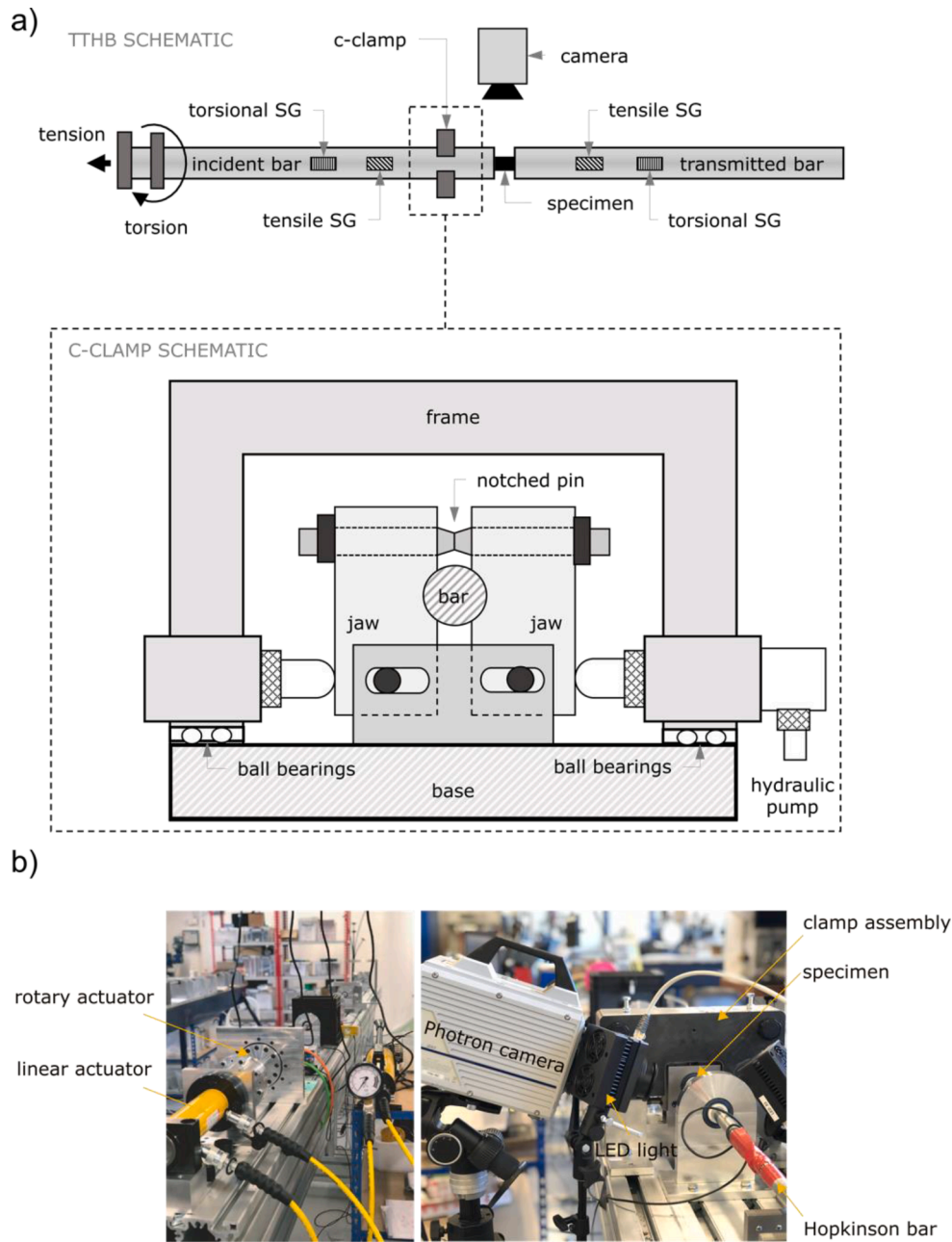


Fig. 2. Schematic (a) and photo (b) of the Tension-Torsion Hopkinson Bar apparatus.

The histories of force and torque are displayed in Fig. 3 for typical experiments including tension loading (Fig. 3a), torsion loading (Fig. 3b), and combined tension-torsion loading (Fig. 3c). The load histories were calculated from wave signals recorded at the incident bar and the transmitted bar and then shifted to the bar-specimen interface known the positions of the strain gauges and the longitudinal and shear wave speeds of the bar material.

As the strain gauges on the incident bar were positioned at the pre-loaded section of the bar, the recorded waves display the initial pre-load and the initiation of the wave. For this reason, the incident waves are termed as ‘stored/release wave’ in Fig. 3. The drop of the initial magnitude to half of the initial load indicates the instant at which the incident wave starts loading the specimen. Since the clamp system was positioned in close proximity to the specimen, the recorded signals correspond to the superposition of the incident wave and the reflected wave. Hence, the curves labelled as stored/released wave represent, from the ‘load release point’, at around 200 microseconds in Fig. 3, the load

applied on the incident side of the specimen, namely Eqs. (1) and (4). The load histories determined from the readings of the strain gauges located on the transmitted bar are the transmitted loads, termed as ‘transmitted wave’ in Fig. 3. These show the load applied on the transmitted side of the specimen, namely Eqs. (2) and (5). Thereafter, the dynamic equilibrium can be directly evaluated by comparing the histories of stored/released wave and transmitted wave.

It is noted that the signal recorded by the shear strain gauge at the incident bar corresponds to the torsional loading of the sample only for the time included between the load release point and the point labelled as ‘A’ in Fig. 3b and Fig. 3c, approximately between 200 and 1000  $\mu$ s. This is because the strain gauge is positioned at the preloaded section of the incident bar, close to the torsional actuator. The recorded signals are therefore the superposition of stored preload stress, release wave, reflected wave and further wave reflections from the fixed end corresponding to the torsional actuator. The comparatively smoother appearance of the shear waves could be attributed to the tight tolerance

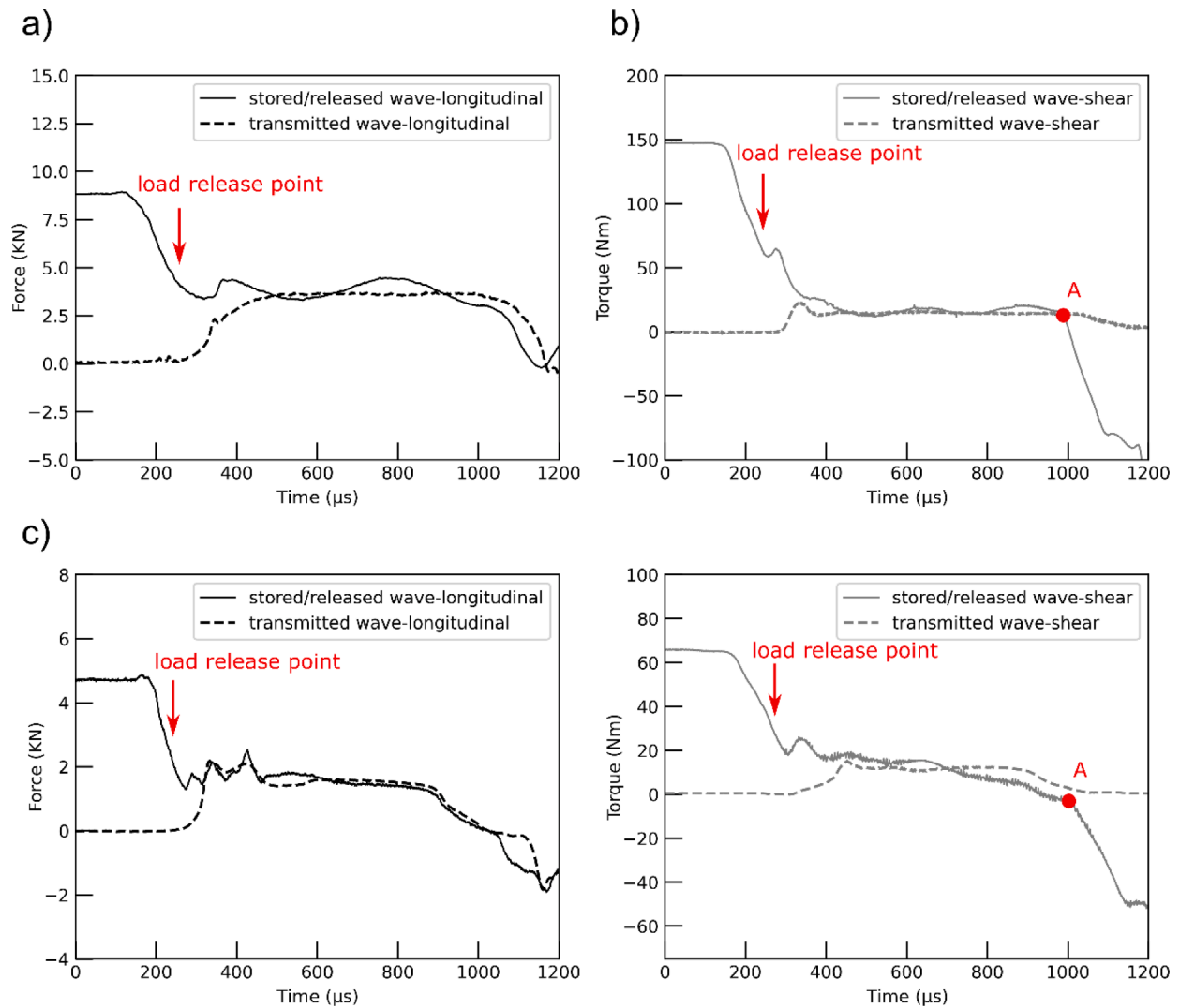


Fig. 3. Dynamic equilibrium of force and torque in typical experiments of (a) tension only, (b) torsion only, and (c) combined tension-torsion loading.

in the octagonal coupling between bar and specimen. On the other hand, the oscillations in the initial part of the longitudinal waves could be in part ascribed to the threaded connection between the bar, specimen and collar.

#### 4. Results and discussion

Table 1 summarises the experiments presented in this study, categorised according to stress state and measured strain rate. The ‘delay’ column quantifies the interval between the arrival of tensile wave and

Table 1

Summary of the quasi-static and dynamic tests conducted under different states of stress and corresponding measured mechanical properties.

Type of test	Specimen label	Biaxial loading angle °	Strain rate $s^{-1}$		Ultimate stress MPa		Percent elongation %		Delay μs
			Tension	Shear	Tension	Shear	Tension	Shear	
Tension	QS1	90.0	0.001		274.0		6.4		
	HR1	90.0	171		393.0		8.2		
	HR2	90.0	129		398.6		8.4		
Torsion	QS2	0.0		0.001		137.0		76.6	
	QS3	0.0		0.001		160.1		63.2	
	HR3	0.0		516		208.0		52.7	
	HR4	0.0		878		213.0		88.4	
	HR5	0.0		1401.		246.1		99.1	
Combined tension-torsion	QS4	49.9	0.001	0.001	210.1	102.2	8.1	11.2	
	QS5	42.5	0.001	0.001	223.4	140.8	13.4	24.5	
	HR6	52.2	669	909	332.1	148.5	20.9	21.9	19
	HR7	50.4	732	760	350.5	167.2	22.1	22.8	16
	HR8	30.5	222	495	180.0	176.6	16.6	36.3	25
	HR9	24.0	526	978	176.2	228.5	24.2	48.2	11

shear wave due to different speeds of sound. The ultimate stresses are the maximum recorded engineering stresses, excluding the initial oscillations due to the dynamic loading.

It is worth emphasising that the experiments labelled as HR1 and HR2 are effectively repetitions of the same loading conditions as variations in the flow stress of Cu beyond  $10^2 \text{ s}^{-1}$  become noticeable only for relatively large differences in the strain rate, as reported in [45]. Similar rate dependence conclusions are reported in [26] for a number of titanium alloys.

To describe the relative contribution of tension and torsion during combined loading, a parameter named biaxial loading angle,  $\beta$ , proportional to the ratio of the measured ultimate tensile stress to the determined ultimate shear stress was introduced as:

$$\tan(\beta) = \frac{\sigma}{\sqrt{3} \tau} \quad (7)$$

Therefore,  $\beta=0^\circ$  corresponds to a torsion-only experiment, whilst  $\beta=90^\circ$  represents a tension-only loading. Any  $\beta$  included between  $0^\circ$  and  $90^\circ$  is representative of arbitrary combinations of tension and torsion, with torsion dominated experiments identified by  $\beta$  lower than  $45^\circ$ . The smaller the biaxial loading angle, the more shear dominated is the experiment.

#### 4.1. Quasi-static experiments

A series of quasi-static combined loading experiments was conducted as a reference to explore the rate-dependence of the material under different stress states. Axial and shear strains were determined via digital image correlation analysis of the pictures recorded by four synchronised cameras. The images were synchronised with the load cells measurements by means of a suitable LabView software.

Tensile and shear stress versus strain responses for tension-only ( $\beta=90^\circ$ ) and torsion-only ( $\beta=0^\circ$ ) are plotted in Figs. 4a and 4b, respectively. A classical ductile fracture behaviour was observed. Strains appear consistent, indicating uniform deformation within the samples. It is noted that an additional quasi-static torsion-only experiment was conducted during this investigation. The response is similar to the one shown in Fig. 4b and is therefore not reported. Since the mechanical properties of pure Cu are highly dependant on microstructure and manufacturing process it is hard to compare the measurements herein reported with those in the literature. As a reference, tensile strength and elongation reported in previous research [15,46-48] range between 100 MPa and 400 MPa and between 5% and 50% respectively. The ultimate shear strength varies between 70 MPa and 175 MPa while the shear

strain to failure is included between 60% and 90%.

Fig. 5 presents the quasi-static combined tension-torsion response measured from experiments #QS4,  $\beta=49.9^\circ$  and #QS5,  $\beta=42.5^\circ$ . The tensile flow curves show a significant strain hardening until 4% and 8% strain, with a strain to failure approximately equal to 8% and 13% for  $\beta=49.9^\circ$  and  $\beta=42.5^\circ$ , respectively. The shear stress-strain curves reached the ultimate stress soon after the yielding point and then underwent large plastic deformation until failure at strains of about 11% and 24%, respectively. It is noted that the failure strains for the experiment QS4 and QS5 are different, particularly in terms of shear strain. Although the biaxial angle is not substantially different in the two cases the variation in the values of failure strain may be attributed to the distinct deformation mechanisms associated with tension dominated combined loading ( $\beta=49.9^\circ$ ) and torsion dominated combined loading ( $\beta=42.5^\circ$ ). Compared with the tension-only or torsion-only cases, the combined-loading cases present a compromise in terms of the level of tensile and shear stresses measured at a given strain. This is explained by the different stress states induced by the concurrent action of longitudinal and shear loading. Besides, the tensile strain to failure increased slightly when compared to the case of simple tension, whereas the failure strain in shear decreased considerably when compared to the case of simple torsion.

#### 4.2. High-rate experiments

This section of the manuscript presents the experimental results measured during dynamic experiments. Deformation and failure were observed by using a Photron SA5 high-speed camera positioned perpendicularly to the axis of the sample. The results presented in this section display strain histories obtained by means of DIC analysis of the high-speed camera images and stress histories measured by strain gauges located on the transmitted bars. These were synchronised to delineate the stress-strain characteristics of the material under different loading conditions.

Tension only ( $\beta=90^\circ$ ) and torsion only ( $\beta=0^\circ$ ) tests were conducted first. The measured stress-strain responses are illustrated in Fig. 6 and Fig. 7, respectively. The time histories of engineering stress, engineering strain and strain rate for the tension only ( $\beta=90^\circ$ ) test are presented in Fig. 6a; The corresponding stress - strain characteristic is plotted in Fig. 6b. The average strain rate, determined from the slope of the strain history, was calculated as  $171 \text{ s}^{-1}$ . Yielding occurred at a stress of approximately 375 MPa. The onset of failure (around 0.082 strain) was identified by observing, with high speed imaging, the development of a visible crack on the surface of the specimen; at this point the stress

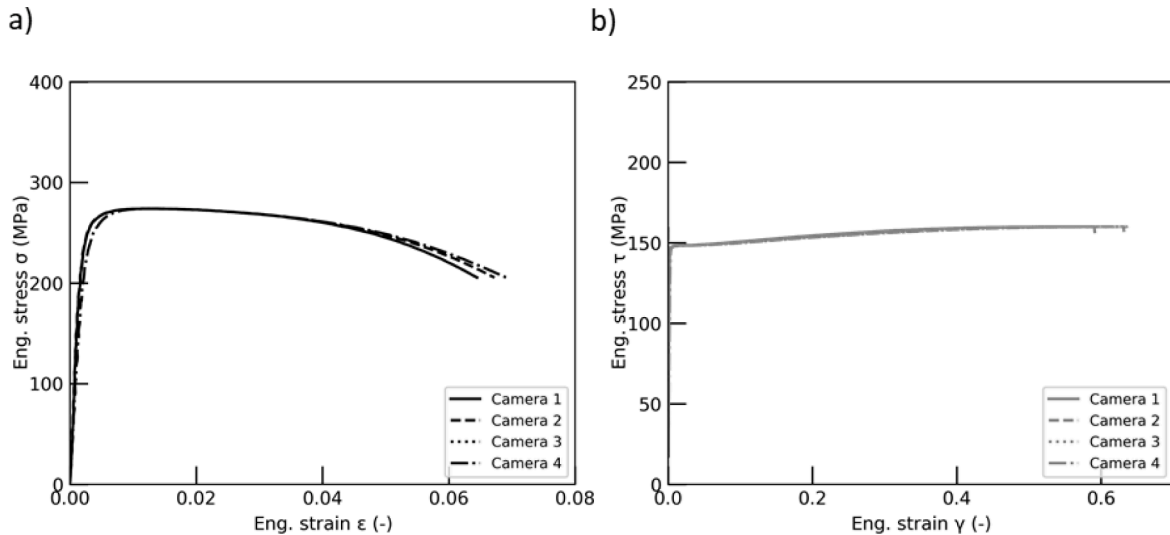


Fig. 4. Quasi-static stress-strain responses for (a) tension-only (#QS1  $\beta=90^\circ$ ) and (b) torsion-only (#QS3  $\beta=0^\circ$ ) experiments.

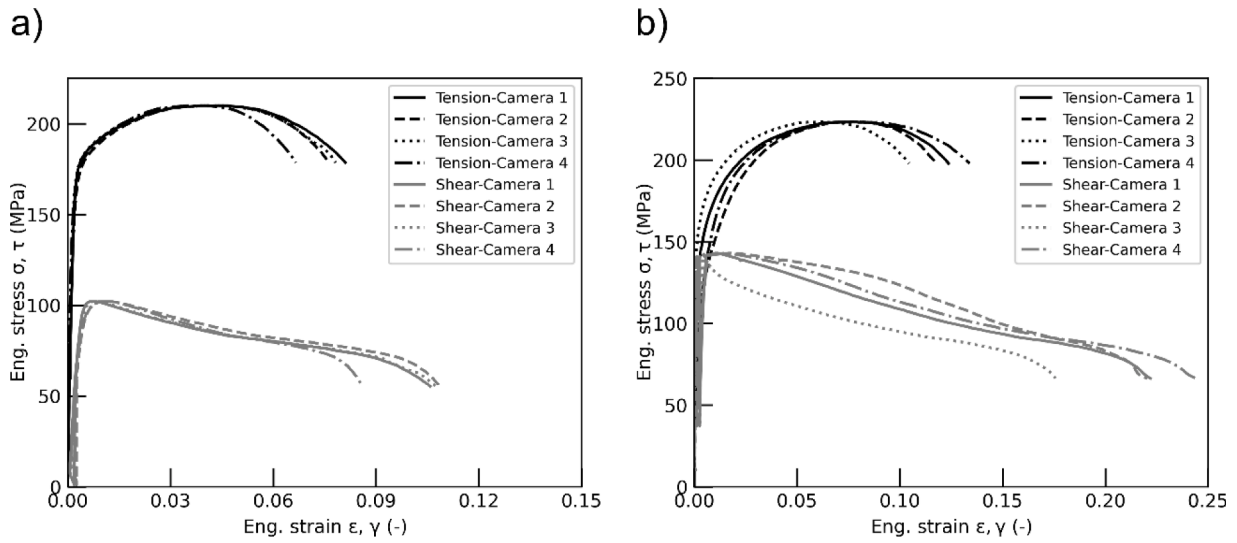


Fig. 5. Quasi-static stress-strain curves from combined tension-torsion experiments: (a) #QS4  $\beta = 49.9^\circ$  and (b) #QS5  $\beta = 42.5^\circ$ .

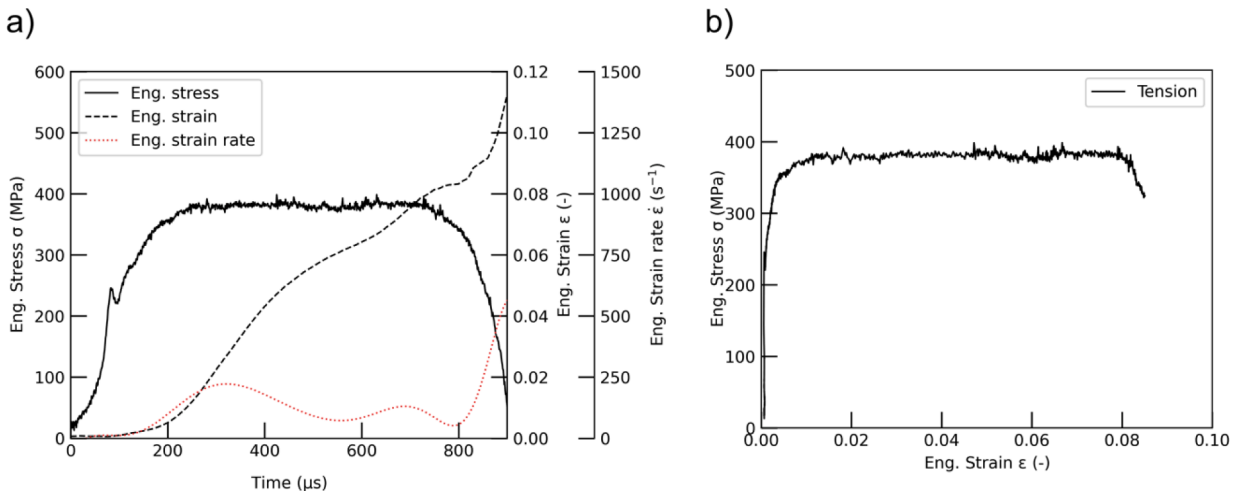


Fig. 6. Dynamic tension-only loading experiment (#HR1,  $\beta = 90^\circ$ , strain rate  $171 \text{ s}^{-1}$ ): (a) Engineering stress, strain and strain rate histories, (b) Engineering stress - strain characteristic.

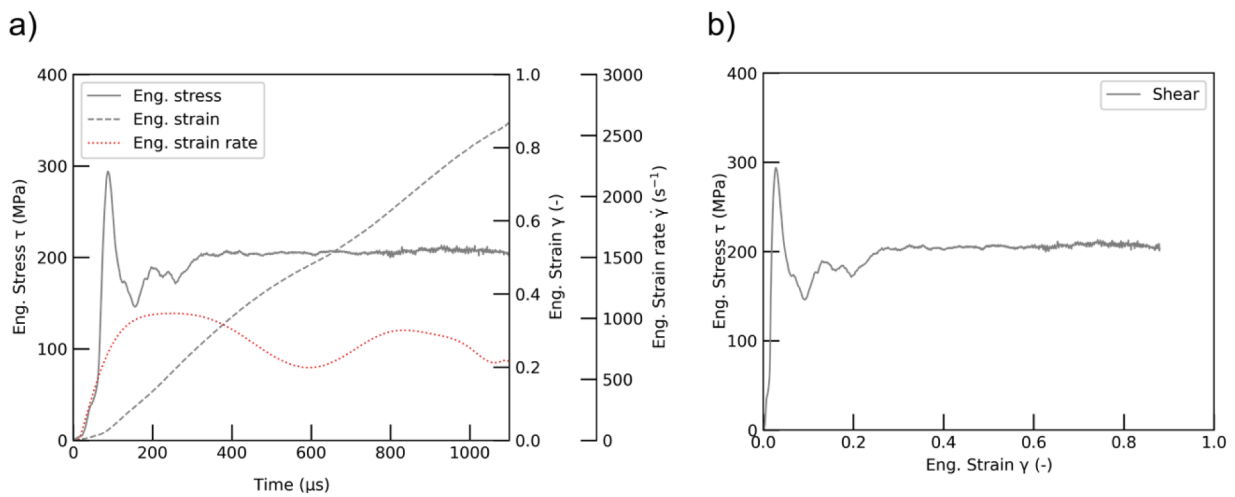


Fig. 7. Dynamic torsion-only loading test (#HR4,  $\beta = 0^\circ$ , strain rate  $878 \text{ s}^{-1}$ ): (a) Engineering stress, strain and strain rate histories, (b) engineering stress - strain characteristic.

dropped rapidly, with a corresponding swift increase of the measured strain. The comparison with the quasi-static test reported in Fig. 4a highlights a considerable increase in yield stress and ultimate stress, while the engineering strain to failure remained comparable, with a slight increase from approximately 6.4% to 8.2% from quasi-static to high rates of strain. In the literature, compressive yield stresses in the range of 300–600 MPa measured at a strain rate of 1200–3800  $\text{s}^{-1}$  were reported by Smirnov and Konstantinov [49] for pure Cu samples of different heat treatment; Ma et al. [50] conducted tensile tests on pure Cu bars and measured tensile stress to be 175–250 MPa at a strain rate of 500–1750  $\text{s}^{-1}$ .

Similarly, the engineering stress, engineering strain and strain rate histories for the torsion-only ( $\beta=0^\circ$ ) experiment are shown in Fig. 7a. The stress-strain characteristic is shown in Fig. 7b. The measured strain rate oscillates around an average value equal to 878  $\text{s}^{-1}$ , determined from the gradient of the strain history. Failure was observed at around 0.884 strain. Similar to the tension-only tests, Cu specimen exhibited observable strain rate sensitivity when subjected to torsional loading with an increase of 40–80 MPa in the ultimate shear stress. As a reference, Xu et al. [48] conducted dynamic shear tests at strain rates up to 45,000  $\text{s}^{-1}$  and temperatures ranging between 293 K and 673 K and found that the yield stress was between 200 MPa and 400 MPa with failure shear strain  $\gamma$  comprised between 80–180%.

It is noted that the early oscillation in the plastic region of the measured shear stress-strain curve is not representative of the dynamic behaviour of the material under investigation, but it is due to the mechanical interaction between the bars and the specimen. Specifically, in the presented high rate torsion experiments, this is caused by the initial minor slack and subsequent abrupt contact interaction at the octagonal coupling between specimen and output bar. Similar oscillations are

reported in [24,51–52].

The mechanical response and stress-strain histories of a representative tension-dominated combined loading high strain rate experiment (#HR6,  $\beta=52.2^\circ$ ) are presented in Fig. 8. The strain rate histories presented in Fig. 8a,b show that the measured longitudinal and shear strain rates were approximately stable during plastic deformation. Stress and strain responses in (a) & (b) were combined to depict the engineering stress-strain curves shown in Fig. 8c. The combined longitudinal and shear responses of the specimen displayed a typical ductile behaviour; the linear elastic phase and first yield are followed by plastic deformation with negligible strain hardening, and subsequently by progressive damage and failure. Fig. 9 illustrates the typical progressive deformation and failure of two combined tension-torsion high rate experiments with tensile (#HR6) or shear (#HR9) loading dominant. It is noted that the failure appears as a crack located in the middle of the gauge section and perpendicular to the longitudinal axis of the sample.

One of the important aspects of the dynamic combined tension-torsion experiments is the wave synchronization between longitudinal and shear waves as these propagate at different speeds. This was accessed by probing the instants at which the tensile and torsional incident waves reach 20% of their maximum amplitude. The slight delay, in the order of tens of microseconds between longitudinal and shear waves (Table 1), could be attributed to the different release mechanisms of the corresponding stored energies, and it is consistent with what reported by Lewis and Goldsmith [37]. It must be stressed that a perfect synchronization of the loading pulses does not guarantee an absolutely synchronized deformation of the sample; Indeed, as the two waves travel at different speeds both in the elastic and plastic regimes, they cannot propagate along the specimen unitedly regardless of whether they reach the specimen interface simultaneously.

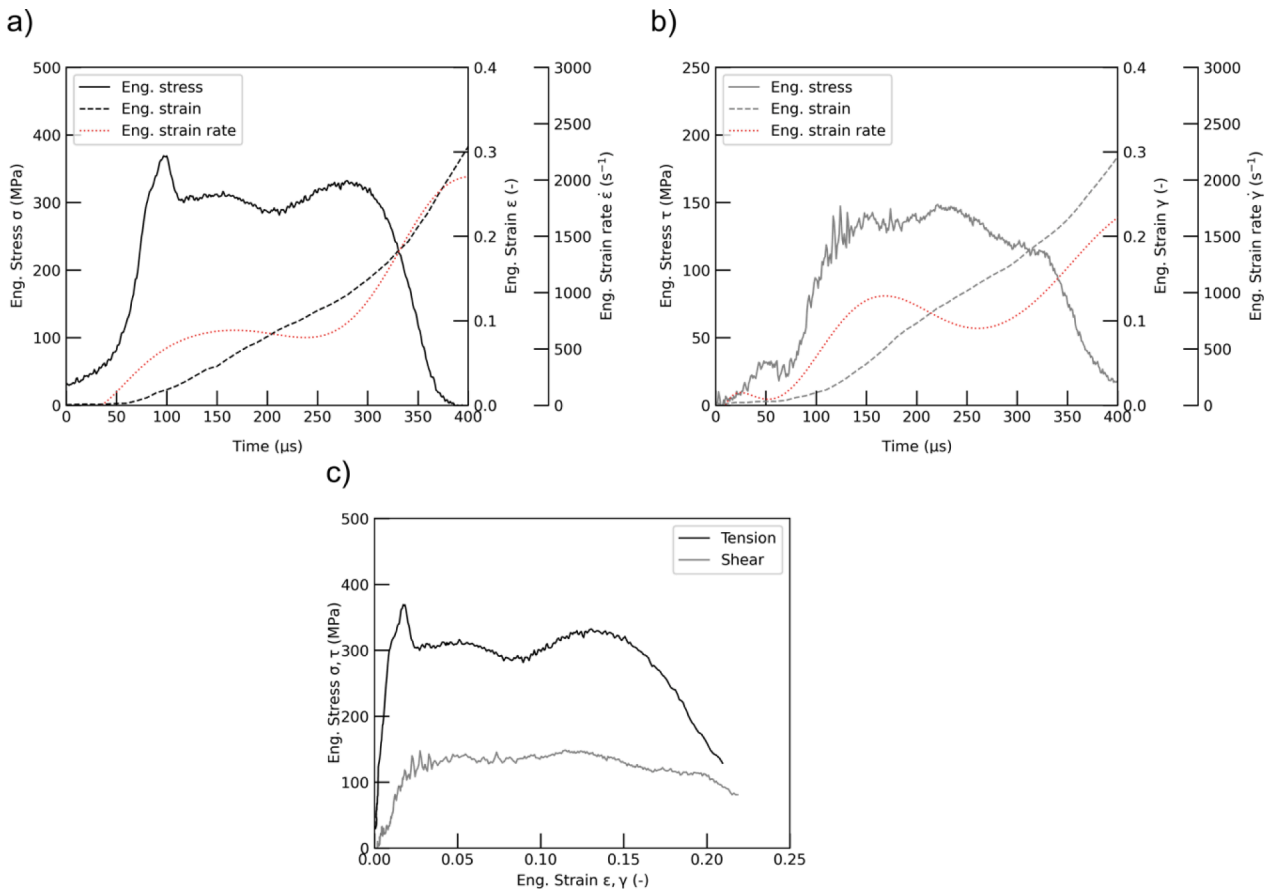


**Fig. 8.** Combined tension-torsion loading dynamic test (#HR6,  $\beta=52.2^\circ$ ): (a) Engineering stress, strain and strain rate histories of tensile loading; (b) Engineering stress, strain and strain rate histories of torsional loading; (c) Engineering stress-strain characteristics.

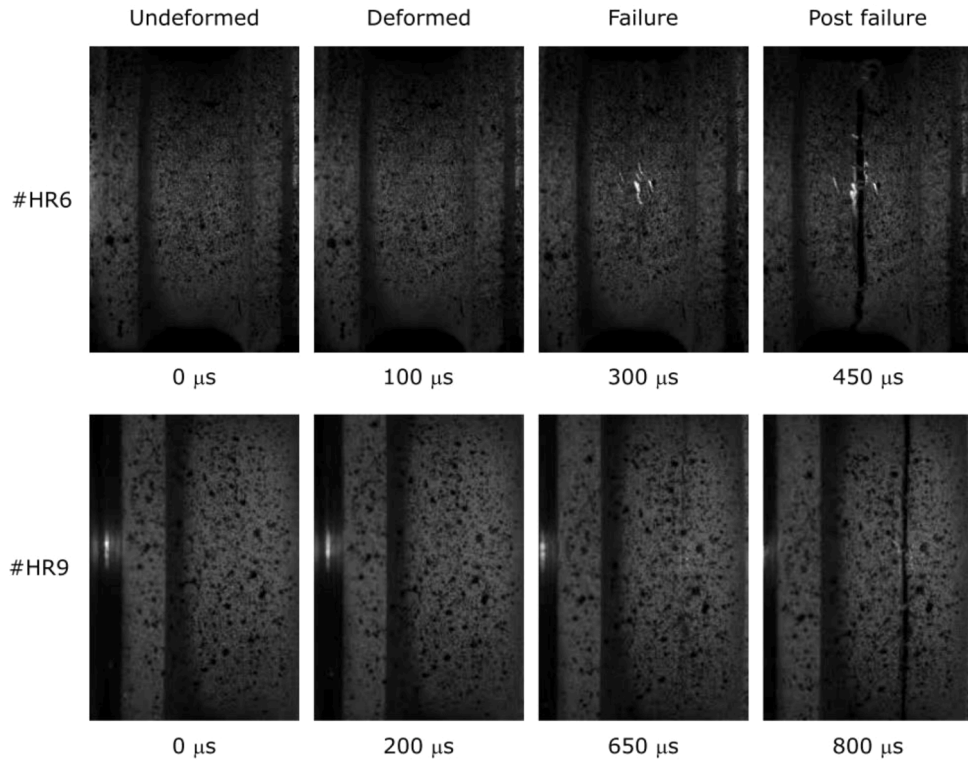


Fig. 9. Progressive deformation and failure of combined tension-torsion experiments (#HR6  $\beta=52.2^\circ$  and #HR9  $\beta=24.0^\circ$ ).

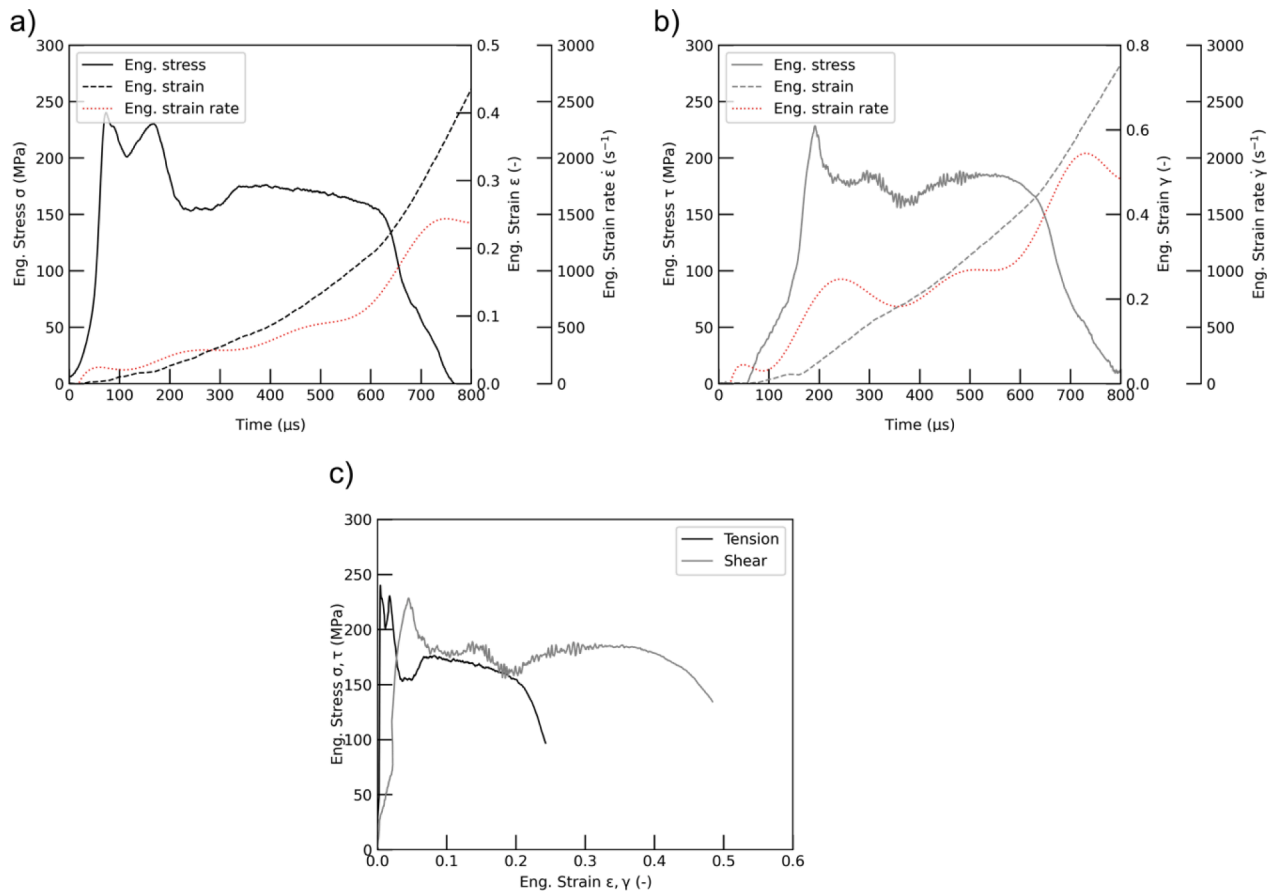


Fig. 10. Combined tension-torsion loading dynamic experiment (#HR9,  $\beta=24.0^\circ$ ): (a) Engineering stress, strain and strain rate histories of tensile loading; (b) Engineering stress, strain and strain rate histories of torsional loading; (c) Engineering stress-strain characteristics.

The experimental results for a representative shear dominated tension-torsion experiment ( $\#HR9$ ,  $\beta=24.0^\circ$ ) are illustrated in Fig. 10. Here, despite the oscillation between  $300 \mu s$  and  $400 \mu s$ , the shear strain rate appears to be steadier than the tensile strain rate; The different trends in the tensile and shear strain rates histories are presumably due to the different release mechanisms of the stored tensile and torsional energies. the failure of the specimen is identified by the simultaneous drop in tensile and shear stress, as presented in Fig. 10a,b. The measured stress and strain histories are combined to depict the engineering stress-strain characteristics reported in Fig. 10c, describing a typical ductile behaviour. The failure mode developed at this biaxial loading angle was not significantly different from that described for the specimen  $\#HR6$ , as shown in Fig. 9, with the crack appearing as an approximately straight line characterised by a mild curvature due to the presence of shear stress.

A summary of the measured dynamic stress-strain responses, categorised by the biaxial loading angle  $\beta$ , is presented in Fig. 11. The tensile characteristics are plotted in Fig. 11a where the black solid lines correspond to the tension only high rate experiment ( $\beta=90^\circ$ ). The shear characteristics are summarized in Fig. 11b where the red lines represent the torsion only dynamic experiment ( $\beta=0^\circ$ ). The curves identified by  $\beta$  included between  $0^\circ$  and  $90^\circ$  represent different combinations of tension-torsion loads. In both figures, the blue curves indicate a tension dominated experiment, whereas the orange curves indicate that the shear stress is prevailing. It can be concluded from Fig. 11a,b that for a given

loading case the proportion between tensile stress and shear stress is related to the biaxial loading angle  $\beta$ . The ultimate tensile stress decreases as the ultimate shear stress increases, i.e. when the angle  $\beta$  diminishes. Similarly, the shear failure strain increases as the contribution of the shear stress to the equivalent stress becomes more important, while the tensile failure strain appears to be less sensitive to the variation in  $\beta$ .

It is worth stating that the oscillations present in some of the reported stress-strain characteristics ( $\beta = 0^\circ$ ,  $\beta = 24.0^\circ$ ,  $\beta = 50.4^\circ$  and to a smaller extent  $\beta = 52.2^\circ$ ) at the early stages of the plastic region are not attributed to the dynamic behaviour of the material but to the interactions between bars, collars, octagonal studs and the specimen during dynamic loading. Specifically, these initial fluctuations are ascribed to the initial minor slack between the connections and the subsequent abrupt contact interaction with the specimen. Moreover, the rapid release of the clamp storing the tensile and torsional elastic energy in the incident bar may introduce moderate vibrations that can affect the measured signals. Comparable oscillations are presented in [51–54].

Fig. 11c describes the path of the measured engineering normal and shear strains during all high strain rates experiments; It is evident that evolution of direct and shear strains is nearly proportional as indicated by the approximately linear trend of the charts. This is explained by the fact that a nearly constant strain rate was achieved both in tension and torsion during dynamic loading, hence the practically constant ratio between normal and shear strains.

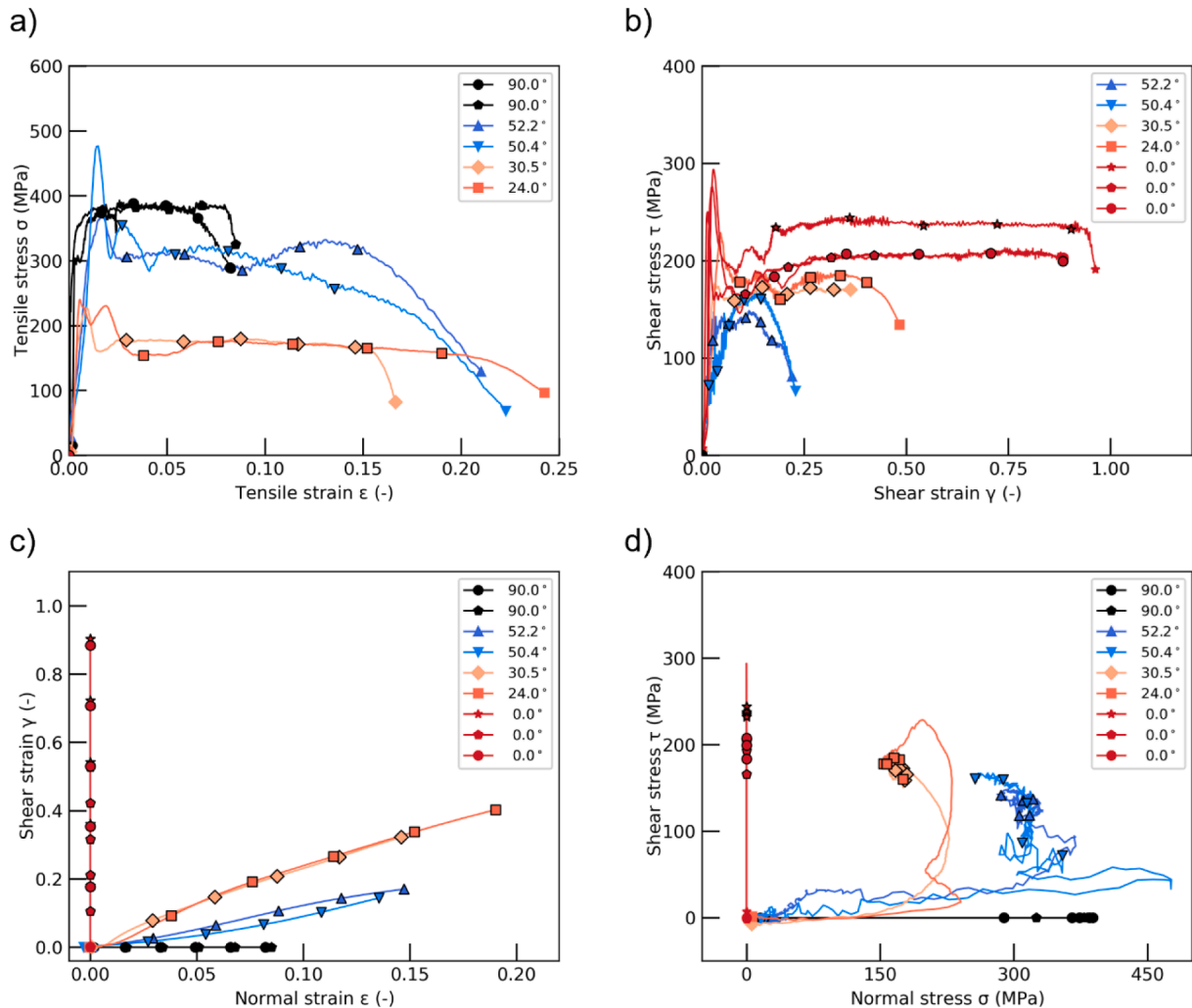


**Fig. 11.** Summary of high strain rate tests: engineering stress vs strain curves for (a) tension; (b) shear; loading trajectories of (c) shear strains versus normal strain; (d) shear stress versus normal stress.

Fig. 11d illustrates the trajectories described by normal and shear stresses during dynamic loading. These appear significantly more irregular due to the inherent oscillations in the measured stress waves and different stress wave propagation velocities. However, the analysis of the plastic regime of deformation reveals a fairly stable ratio between normal and shear stresses. This is visualised by locating a number of points in the plastic region of the stress-strain curves reported in Fig. 11a,b. These are labelled using different markers for each biaxial angle  $\beta$  and are equally spaced in strain between the yield and failure points. It is evident that, while the same points appear uniformly distributed along the trajectories of strain (Fig. 11c), they are positioned only at the tail of the stress trajectories (Fig. 11d). This indicates that the irregular portion of the stress paths depicted in Fig. 11d is only associated with the early stages of loading up to the yield point, and that the proportion between direct and shear stresses is relatively steady in the plastic regime. Additionally, it is noted that the first part of the stress trajectories is characterised by a nearly horizontal trend for all combined loading experiments, regardless of if the loading is tensile or shear dominated. This is explained by the fact that, in this initial phase, the tensile stress is characterised by higher magnitude than the shear stress, due to the higher wave propagation velocity of the longitudinal waves in comparison to the shear waves.

#### 4.3. Multiaxial failure stress envelopes

This section presents a summary of the measured experimental results. To better understand the failure of pure Cu under combined loading conditions Fig. 12 depicts its failure locus as a function of ultimate tensile and shear stresses at quasi static and dynamic rates of strain. The Drucker-Prager (D-P) criterion [55] is employed to approximate the experimental failure envelopes. The criterion, a three-dimensional pressure dependant model can be written in compact form as follows:

$$\sqrt{J_2} = A + BI_1 \quad (8)$$

where  $J_2$  is the second invariant of the deviator stress tensor,  $I_1$  is the first invariant of the stress tensor, A and B are material constants to be determined from the experimental data.

The constants A and B are determined via least square optimisation. Thus, the equations describing the strength of pure Cu subjected to combined tension-torsion at quasi-static ( $10^{-3} \text{ s}^{-1}$ ) and high strain rate ( $10^2 \text{ s}^{-1}$ – $10^3 \text{ s}^{-1}$ ) are determined as in equations 1.9 and 1.10

respectively:

$$\sqrt{J_2} = 157 - 0.039 I_1 \quad (9)$$

$$\sqrt{J_2} = 239 - 0.058 I_1 \quad (10)$$

These allow to determine whether the material has failed when subjected to a given state of stress and rate of strain. The increase of the coefficient A from 157 MPa, in quasi static regime, to 220 MPa, in dynamic loading conditions, denotes an evident rate dependence of the material strength. The relatively small negative values of the coefficient B predict a moderate asymmetry of the uniaxial ultimate stresses in tension ( $\sigma_t$ ) and compression ( $\sigma_c$ ), quantifiable by the ratio:

$$\frac{\sigma_c}{\sigma_t} = \frac{1 - \sqrt{3} B}{1 + \sqrt{3} B} \quad (11)$$

equal to 1.14 and 1.22 for the quasi static and the dynamic strain rate respectively [56–57]. It is worth noting that this ratio refers to the engineering values of the ultimate stresses. The small variation of the coefficient B with the strain rate indicates an approximately concentric expansion of the D-P failure envelope from the quasi static to the dynamic loading regime. The minor deviation from the dynamic D-P envelope of the data point corresponding to the dynamic tension experiment is explained by the lower strain rate measured in this experiment ( $171 \text{ s}^{-1}$ ) in comparison to the other dynamic loading cases.

#### 4.4. Fracture morphology

The deformation and failure under different stress states and strain rates were further investigated analysing the fracture surfaces of the samples by means of SEM imaging. The SEM micrographs were recorded using a Merlin Field Emission Gun-Scanning Electron Microscope (FEG-SEM) from Carl Zeiss. A Secondary electron detector (SE) was used for all the images, at a voltage of 20 kV with a working distance of 9.00 mm.

Fig. 13 illustrates the fracture morphologies of pure Cu samples deformed in quasi-static loading conditions. The fracture surface characteristics include a specimen deformed and failed under tensile stress ( $\beta = 90^\circ$ , Fig. 13a-d) and one sample loaded under shear dominated combined loading ( $\beta = 42.5^\circ$ , Fig. 13e, f). It is noted that the quasi-static torsion specimens did not fracture into two separate parts. Consequently, as the fracture surface of these could not be accessed without damaging the microstructure of the fracture plane, the failure surface for

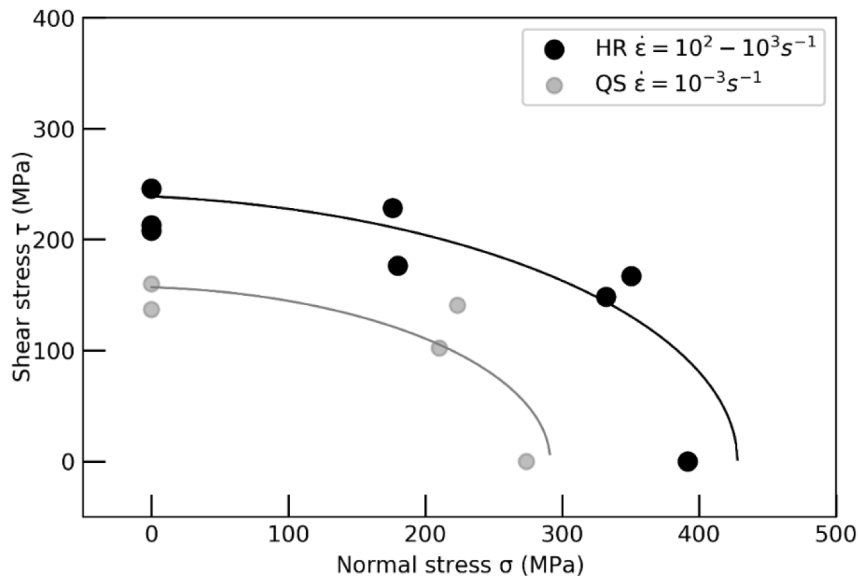
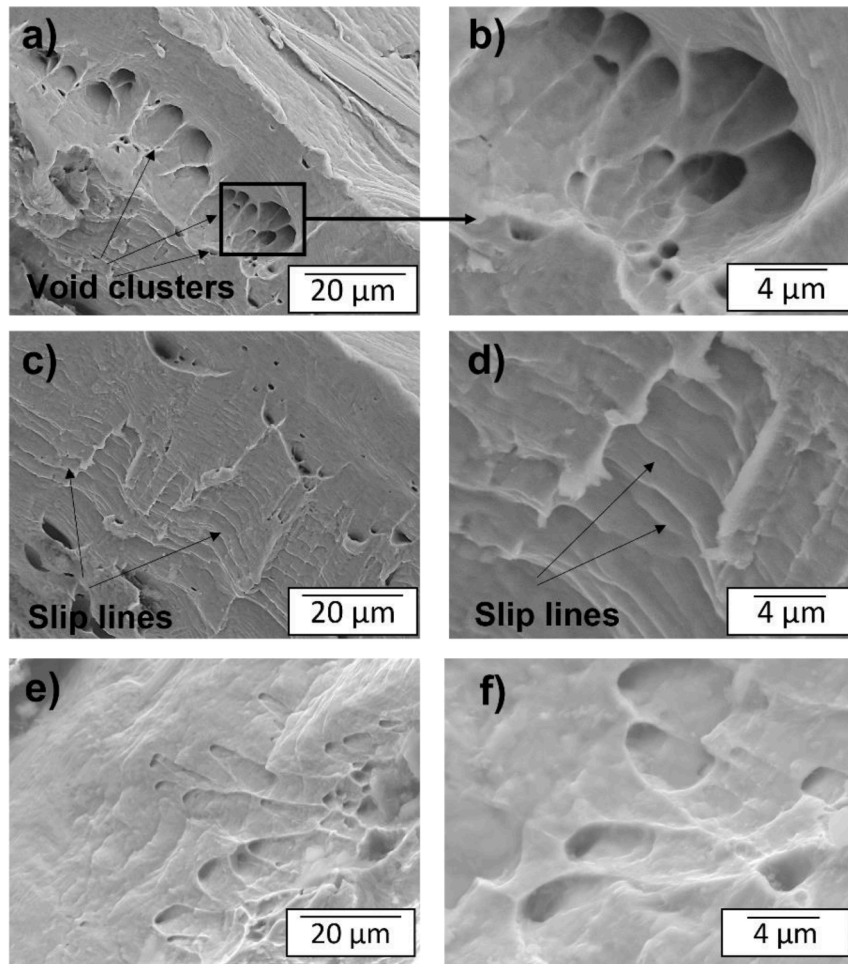


Fig. 12. Failure stress locus of commercially pure Cu at quasi-static and dynamic rates of strain.



**Fig. 13.** Scanning electron micrographs of the fracture morphology of commercially pure copper under quasi-static loading: (a,b,c,d) tension and (e,f) tension-dominated combined loading.

the case of pure torsion is not presented.

The examination of the tensile specimen ( $\beta = 90^\circ$ ) surface reveals a line of void clusters along a circumference close to the outer wall of the sample. Micro-voids together with larger and deeper voids of approximately  $4\ \mu\text{m}$  in diameter are observed. It is likely that the voids have nucleated, grown and coalesced in regions of stress concentration. Adjacent to the voids, closer to the internal wall of the sample, slip appears to be the dominating plastic deformation mechanism. This is emphasised by the presence of what appear to be slip lines, arrowed and magnified in Fig. 13c and Fig. 13d.

The fracture surface of a sample deformed and failed in combined tension-torsion loading ( $\beta = 42.5^\circ$ ) is shown in Fig. 13e and Fig. 13f. The influence of the stress state on the failure surface is manifested by the occurrence of shallower and more elongated dimples attributable to the presence of the shear load.

The fracture surfaces of the dynamically loaded specimens are shown in Fig. 14. The micrographs, displayed at two different magnifications, illustrate the failure surface morphology for four representative stress states: tension ( $\beta = 90^\circ$ , Fig. 14a,b), tension dominated combined load ( $\beta = 50.4^\circ$ , Fig. 14c,d), torsion dominated combined load ( $\beta = 30.5^\circ$ , Fig. 14e,f), and torsion ( $\beta = 0^\circ$ , Fig. 14g,h).

The fracture characteristic of the high rate tensile specimen (Fig. 14a) presents a lower void density compared to its quasi-static counterpart (Fig. 13a), with the micro-voids characterised by a much smaller size. It can be therefore inferred that the strain rate has a significant effect on void nucleation and growth in pure copper. At quasi-static strain rates, the material has more time to accommodate the

plastic strain, therefore, more micro-voids can nucleate and grow.

The combined loading sample of biaxial loading angle  $\beta = 50.4^\circ$  (Fig. 14c,d) features deep and elongated dimples orientated intermediately between the radial and the circumferential directions. The elongated shape is attributed to the shear deformation. This is confirmed by the failure surface morphology of the sample deformed at high strain rate under torsion-dominated combined loading ( $\beta = 30.5^\circ$ , Fig. 14e,f), displaying elongated dimples orientated in the circumferential direction. Analogous features are visible on the fracture surface corresponding to the sample loaded in torsion ( $\beta = 0^\circ$ , Fig. 14g,h).

It is evident that the stress state has a direct influence on the fracture surface morphology of the examined samples. In general, larger and elongated dimples are observed as the biaxial angle decreases, i.e., as the shear load dominates. Moreover, larger and more elongated dimples also indicate a higher fracture strain [58]. This is in agreement with the macroscopic mechanical behaviour measured on the commercially pure copper investigated, as larger failure strains were obtained when torsion prevailed during combined loading.

## 5. Conclusion

The present investigation details the rate dependant mechanical behaviour and failure stress locus of commercially pure Cu subjected to arbitrary combinations of concurrent tension and torsion loading. The main conclusions of this study are summarised below.

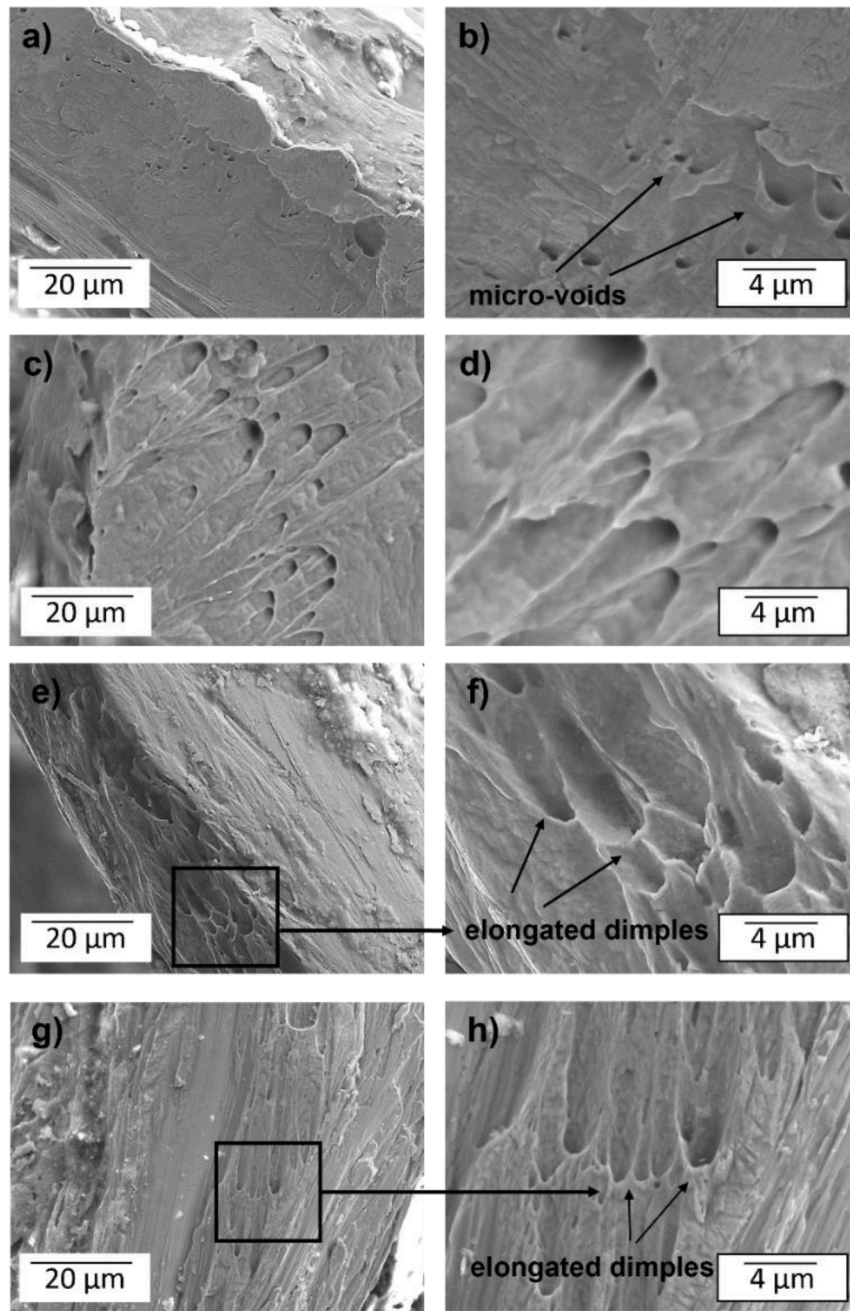


**Fig. 14.** Scanning electron micrographs of the fracture morphology of commercially pure copper under high rate loading: (a,b,) tension loading; (c,d) tension-dominated combined loading; (e,f) torsion-dominated combined loading; (g,h) torsion loading.

### 5.1. Experimental technique and loading path analysis

A novel Split Hopkinson Tension-Torsion Bar capable of generating, in a single loading case, tensile and torsional stress waves was developed. A series of dynamic combined loading experiments were conducted on commercially pure copper. The analysis of the high-rate experiments demonstrates the synchronisation of direct and shear stress waves upon loading of the sample and the capability of the apparatus of achieving dynamic equilibrium conditions.

The assessment of the dynamic loading paths shows that direct and shear strains were nearly proportional during deformation. The evolution of the stress trajectories during tension-torsion dynamic loading describes complex trajectories that are, nonetheless, characterised by an approximately steady proportion between normal and shear stresses in the plastic regime.

### 5.2. Failure analysis and rate dependence

The measured experimental results outline the failure stress locus of commercially pure copper under different combinations of direct and shear stress, including shear, shear dominated tension-shear, tension dominated tension-shear and plain tension. The quasi static and dynamic failure loci are presented in the direct-shear stress space to motivate novel theoretical constitutive models.

The Drucker-Prager (D-P) criterion was employed to approximate the experimental failure envelopes and to quantify the rate sensitivity of Cu. The resulting quasi static and dynamic D-P loci allow determining whether the material has failed when subjected to a given state of stress and rate of strain. The material shows an apparent rate dependant behaviour as its failure stress locus expands in a proportional manner with the increase of strain rate. A moderate asymmetry of the uniaxial

ultimate stresses in tension and compression is predicted both at quasi-static and dynamic strain rates.

The post-mortem analysis of the fracture surfaces of the samples illustrates the effect of the biaxial loading angle  $\beta$  on the fracture morphology. It was observed that the stress state affects the failure surface characteristics of the examined samples. In general, larger and elongated dimples are detected as the biaxial angle decreases, i.e., as the shear load prevails.

Future research will investigate the influence of the high rate loading path, i.e. the tension-torsion loading sequence, on the dynamic behaviour of engineering materials.

#### CRedit authorship contribution statement

**Junyi Zhou:** Investigation, Visualization, Formal analysis, Validation, Writing – original draft. **Yuan Xu:** Conceptualization, Methodology, Investigation, Formal analysis, Visualization, Writing – review & editing. **Maureen Aceves Lopez:** Formal analysis. **Lukasz Farbaniec:** Writing – review & editing. **Sophoclis Patsias:** Project administration. **Duncan Macdougall:** Writing – review & editing. **Julian Reed:** Resources. **Nik Petrinic:** Resources. **Daniel Eakins:** Resources. **Clive Siviour:** Resources. **Antonio Pellegrino:** Conceptualization, Supervision, Funding acquisition, Project administration, Writing – review & editing.

#### Declaration of Competing Interest

The authors declare that they have no known competing financial interests or personal relationships that could have appeared to influence the work reported in this paper.

#### Acknowledgements

The authors would like to thank Rolls-Royce plc and the EPSRC for the support under the Prosperity Partnership Grant\Cornerstone: Mechanical Engineering Science to Enable Aero Propulsion Futures, Grant Ref: EP/R004951/1. Additionally the authors are grateful to S. Carter, J. Fullerton, D. Robinson and P. Tantrum for their assistance in the manufacturing of the apparatus and to Dr. David Townsend for the enlightening discussions during the experimentation.

#### References

- Ungár T, Tóth LS, Illy J, Kovács I. Dislocation structure and work hardening in polycrystalline OFHC copper rods deformed by torsion and tension. *Acta Metall* 1986;34(7):1257–67.
- Gu J, Ni S, Song M. Effects of torsional deformation on the mechanical properties and microstructures of a commercial pure copper. *J Mater Eng Perform* 2019;28(1):543–8.
- Wang C, Li F, Wei L, Yang Y, Dong J. Experimental micro-indentation of pure copper subjected to severe plastic deformation by combined tension–torsion. *Mater Sci Eng* 2013;571:95–102.
- Dragnevski KI, Pellegrino A, Heard R, Siviour CR, Mullis AM, Cochrane RF. Mechanical behaviour of rapidly solidified copper: effects of undercooling and strain rate. *Mater Sci Technol* 2020;36(2):202–9.
- Wang Y, Chen M, Zhou F, Ma E. High tensile ductility in a nanostructured metal. *Nature* 2002;419(6910):912–5.
- Nieman GW, Weertman JR, Siegel RW. Mechanical behavior of nanocrystalline Cu and Pd. *J Mater Res* 1991;6(5):1012–27.
- Sanders PG, Eastman JA, Weertman JR. Elastic and tensile behavior of nanocrystalline copper and palladium. *Acta Mater* 1997;45(10):4019–25.
- Wang YM, Ma E. Temperature and strain rate effects on the strength and ductility of nanostructured copper. *Appl Phys Lett* 2003;83(15):3165–7.
- Zhao C, Li F, Li J, Ma X, Wan Q, Tong T. Influence of deformation stress triaxiality on microstructure and microhardness of pure copper processed by simultaneous torsion and tension. *J Mater Eng Perform* 2017;26(8):4104–11.
- Lindholm US, Nagy A, Johnson GR, Hoegfeldt JM. Large strain, high strain rate testing of copper. *J Eng Mater Technol* 1980;102(4):376–81.
- Tong W, Clifton RJ, Huang S. Pressure-shear impact investigation of strain rate history effects in oxygen-free high-conductivity copper. *J Mech Phys Solids* 1992;40(6):1251–94.
- Gray III GT, Lowe TC, Cady CM, Valiev RZ, Aleksandrov IV. Influence of strain rate & temperature on the mechanical response of ultrafine-grained Cu, Ni, and Al-4Cu-0.5 Zr. *Nanostruct Mater* 1997;9(1–8):477–80.
- Mishra A, Martin M, Thadhani NN, Kad BK, Kenik EA, Meyers MA. High-strain-rate response of ultra-fine-grained copper. *Acta Mater* 2008;56(12):2770–83.
- Armstrong RW, Arnold W, Zerilli FJ. Dislocation mechanics of copper and iron in high rate deformation tests. *J Appl Phys* 2009;105(2):023511.
- Nemat-Nasser S, Li Y. Flow stress of FCC polycrystals with application to OFHC Cu. *Acta Mater* 1998;46(2):565–77.
- Tanner AB, McGinty RD, McDowell DL. Modeling temperature and strain rate history effects in OFHC Cu. *Int J Plast* 1999;15(6):575–603.
- Hopkinson B. The effects of momentary stresses in metals. *Proc R Soc Lond* 1905;74(497):498–506.
- Hopkinson B. A method of measuring the pressure produced in the detonation of high, explosives or by the impact of bullets. *Philos Trans R Soc Lond Ser A* 1914;213(497–508):437–56.
- Landon JW, Quinney H. Experiments with the Hopkinson pressure bar. *Proc R Soc Lond Ser A* 1923;103(723):622–43.
- Kolsky H. An investigation of the mechanical properties of materials at very high rates of loading. *Proc Phys Soc Lond Sect B* 1949;62(11):676.
- Davies EDH, Hunter SC. The dynamic compression testing of solids by the method of the split Hopkinson pressure bar. *J Mech Phys Solids* 1963;11(3):155–79.
- Gray III GT. Classic split-Hopkinson pressure bar testing. In: Kuhn H, Medlin D, editors. *ASM Handbook, mechanical testing and evaluation*. Ohio: ASM International: Materials Park; 2000. p. 462–76. Vol. 8.
- Kraft JM, Sullivan AM, Tipper CF. The effect of static and dynamic loading and temperature on the yield stress of iron and mild steel in compression. *Proc R Soc Lond Ser A* 1954;221(1144):114–27.
- Pellegrino A, Tagarielli VL, Gerlach R, Petrinic N. The mechanical response of a syntactic polyurethane foam at low and high rates of strain. *Int J Impact Eng* 2015;75:214–21.
- Xu Y, Dai F. Dynamic response and failure mechanism of brittle rocks under combined compression-shear loading experiments. *Rock Mech Rock Eng* 2018;51:747–64.
- Zhang L, Gour G, Petrinic N, Pellegrino A. Rate dependent behaviour and dynamic strain localisation of three novel impact resilient titanium alloys: experiments and modelling. *Mater Sci Eng* 2020;771:138552.
- Tagarielli VL, Deshpande VS, Fleck NA. The high strain rate response of PVC foams and end-grain balsa wood. *Compos Part B* 2008;39(1):83–91.
- Gilat A, Goldberg RK, Roberts GD. Experimental study of strain-rate dependent behaviour of carbon/epoxy composite. *Compos Sci Technol* 2002;62(10–11):1469–76.
- Farbaniec L, Hogan JD, Xie KY, Shaeffer M, Hemker KJ, Ramesh KT. Damage evolution of hot-pressed boron carbide under confined dynamic compression. *Int J Impact Eng* 2017;99:75–84.
- Harding J, Wood EO, Campbell JD. Tensile testing of materials at impact rates of strain. *J Mech Eng Sci* 1960;2(2):88–96.
- Harding J, Welsh LM. A tensile testing technique for fibre-reinforced composites at impact rates of strain. *J Mater Sci* 1983;18(6):1810–26.
- Gerlach R, Kettenbeil C, Petrinic N. A new split Hopkinson tensile bar design. *Int J Impact Eng* 2012;50:63–7.
- Lu YB, Li QM. Appraisal of pulse-shaping technique in split Hopkinson pressure bar tests for brittle materials. *Int J Prot Struct* 2010;1(3):363–90.
- Staab GH, Gilat A. A direct-tension split Hopkinson bar for high strain-rate testing. *Exp Mech* 1991;31:232–5.
- Zhou J, Pellegrino A, Heisserer U, Duke PW, Curtis PT, Morton J, et al. A new technique for tensile testing of engineering materials and composites at high strain rates. *Proc R Soc A* 2019;475:20190310 (2229).
- Pope DP, Vreeland Jr T, Wood DS. Machine for producing square torsion pulses of micro-second duration. *Rev Sci Instrum* 1964;35:1351–5.
- Lewis JL, Goldsmith W. The dynamic fracture and prefracture response of compact bone by split Hopkinson bar methods. *J Biomech* 1975;8:27–40.
- Gilat A, Wu X. Elevated temperature testing with the torsional split Hopkinson bar. *Exp Mech* 1994;34(2):166–70.
- Gilat A. Torsional Kolsky bar testing. In: Kuhn H, Medlin D, editors. *ASM handbook, mechanical testing and evaluation*. Ohio: ASM International: Materials Park; 2000. p. 505–15 (Vol. 8).
- Yu X, Chen L, Fang Q, Jiang X, Zhou Y. A review of the torsional split Hopkinson bar. *Adv Civil Eng* 2018;2018:271974.
- Gilat A, Cheng CS. Testing with the torsional split Hopkinson bar at strain rates above 10,000 1/s. *WIT Trans Built Environ* 1998;35:549–58.
- Macdougall DAS, Harding J. The measurement of specimen surface temperature in high-speed tension and torsion tests. *Int J Impact Eng* 1998;21(6):473–88.
- Zhang L, Townsend D, Petrinic N, Pellegrino A. Measurement of pure shear constitutive relationship from torsion tests under quasi-static, medium, and high strain rate conditions. *J Appl Mech* 2021;88(12):121003.
- Xu Y, Farbaniec L, Siviour C, Eakins D, Pellegrino A. The development of split Hopkinson tension-torsion bar for the understanding of complex stress states at high rate (Eds.). In: Lamberson L, Mates S, Eliasson V, editors. *Dynamic Behavior of Materials Vol. 1. Conference Proceedings of the Society for Experimental Mechanics Series*. Cham: Springer; 2021. p. 89–93.
- Scapin M, Peroni L, Fichera C. Investigation of dynamic behaviour of copper at high temperature. *Mater High Temp* 2014;31(2):131–40.
- Bagherpour E, Qods F, Ebrahimi R, Miyamoto H. Nanostructured pure copper fabricated by simple shear extrusion (SSE): a correlation between microstructure and tensile properties. *Mater Sci Eng* 2017;679:465–75.

- [47] Kumar N, Dhuria GK, Singh R. Evaluation of tensile strength in friction stir welded aluminum alloy 6101-T6 and commercially pure copper joints. *Mater Today* 2018; 5(9):19230–6.
- [48] Xu Z, Liu Y, Hu H, He X, Huang F. Thermo-viscoplastic behavior and constitutive modeling of pure copper under high-strain-rate shear condition. *Mech Mater* 2019; 129:306–19.
- [49] Smirnov I, Konstantinov A. Influence of ultrafine-grained structure produced by equal-channel angular pressing on the dynamic response of pure copper. *Procedia Struct Integr* 2018;13:1336–41.
- [50] Ma D, Chen D, Wu S, Wang H, Hou Y, Cai C. An interrupted tensile testing at high strain rates for pure copper bars. *J Appl Phys* 2010;108(11):114902.
- [51] Kobayashi T, Simons JW, Brown CS, Shockey DA. Plastic flow behavior of Inconel 718 under dynamic shear loads. *Int J Impact Eng* 2008;35(5):389–96.
- [52] Macdougall D, Harding J. Materials testing for constitutive relations. *Jo Phys IV Proc* 1997;7(C3):103–8.
- [53] Mirone G, Corallo D, Barbagallo R. Experimental issues in tensile Hopkinson bar testing and a model of dynamic hardening. *Int J Impact Eng* 2017;103:180–94.
- [54] Mirone G, Barbagallo R, Giudice F, Di Bella S. Analysis and modelling of tensile and torsional behaviour at different strain rates of Ti6Al4V alloy additive manufactured by electron beam melting (EBM). *MaterSci Eng* 2020;793:139916.
- [55] Drucker DC, Prager W. Soil mechanics and plastic analysis or limit design. *Q Appl Math* 1952;10(2):157–65.
- [56] Clyne TW, Campbell JE. Testing of the plastic deformation of metals. Cambridge University Press; 2021.
- [57] Lin P, Hao Y, Zhang B, Zhang S, Chi C, Shen J. Tension-compression asymmetry in yielding and strain hardening behavior of CP-Ti at room temperature. *MaterSci Eng* 2017;707:172–80.
- [58] Verleysen P, Peirs J. Quasi-static and high strain rate fracture behaviour of Ti6Al4V. *Int J Impact Eng* 2017;108:370–88.